Towards Three-Dimensional Weyl-SurfaceSemimetals in Graphene Networks

Article *in* Nanoscale · January 2016

DOI: 10.1039/C6NR00882H · Source: arXiv

Nanoscale

PAPER

View Article Online
View Journal | View Issue

Cite this: *Nanoscale*, 2016, **8**, 7232

Towards three-dimensional Weyl-surface semimetals in graphene networks†

Chengyong Zhong,[a] Yuanping Chen,*[a] Yuee Xie,*[a] Shengyuan A. Yang,[b] Marvin L. Cohen[c] and S. B. Zhang*[d]

Received 31st January 2016,
Accepted 26th February 2016

DOI: 10.1039/c6nr00882h

www.rsc.org/nanoscale

Graphene as a two-dimensional topological semimetal has attracted much attention for its outstanding properties. In contrast, three-dimensional (3D) topological semimetals of carbon are still rare. Searching for such materials with salient physics has become a new direction in carbon research. Here, using first-principles calculations and tight-binding modeling, we propose a new class of Weyl semimetals based on three types of 3D graphene networks. In the band structures of these materials, two flat Weyl surfaces appear in the Brillouin zone, which straddle the Fermi level and are robust against external strain. Their unique atomic and electronic structures enable applications in correlated electronics, as well as in energy storage, molecular sieves, and catalysis. When the networks are cut, the resulting slabs and nanowires remain semimetallic with Weyl lines and points at the Fermi surfaces, respectively. Between the Weyl lines, flat surface bands emerge with possible strong magnetism. The robustness of these structures can be traced back to a bulk topological invariant, ensured by the sublattice symmetry, and to the one-dimensional Weyl semimetal behavior of the zigzag carbon chain.

Introduction

The search for three-dimensional (3D) Weyl semimetals has fueled tremendous interest in condensed matter physics as such matter may provide a versatile platform for investigating the fascinating properties of Weyl states.[1–8] Carbon, being one of the most abundant elements in the universe, is uniquely important, as it may form a basis, and perhaps be the simplest one, to study Weyl physics. This is because carbon has several hybridization states (sp, sp^2 and sp^3).[9,10] Due to the sp^2 hybridization, graphene is, in fact, a two-dimensional (2D) topological semimetal, whose Fermi surface is made of two Fermi points where the conduction and valence bands touch each other with linear energy dispersion.[11,12] Although it is customary to term graphene a Dirac semimetal, it is fundamentally no different from a 2D Weyl semimetal, as the negligibly small spin–orbit coupling (SOC) strength makes it possible to treat the electron spin as a dummy variable.[13] This raises the prospect of Weyl-like semimetals made of purely 3D carbon networks.

In fact, the theoretical search for the 3D carbon networks has been intense, fueled by their potential outstanding properties. This includes the proposed sp^3-hybridizated M-carbon,[14] carbon Kagome lattice (CKL),[15] sp^2-hybridizated H6-carbon,[16] bct-4,[17] and sp^2/sp^3-hybridizated T6-carbon,[18] and Squaroglitter.[19] While these carbon allotropes are all non-semimetals, a graphene network, termed Mackay–Terrones crystal, has been proposed to be a topological nodal-line semimetal.[20] Another interpenetrated graphene network (IGN) has been identified as a Weyl-loop semimetal.[21] Recent experiments indicate that indeed 3D graphene networks can be good candidates for semimetals. For example, an interconnected graphene network grown by chemical vapor deposition showed a very high electrical conductivity which could be six orders of magnitude higher than that of the chemically-derived graphene-based composites.[22]

In this paper, we propose a different class of carbon-based topological semimetals, consisting of Weyl surfaces as their Fermi level. They are made of two kinds of graphene nanoribbon-like structural motifs: in the first kind in Fig. 1(a), all (green) carbon atoms are sp^2-like. In the second kind in Fig. 1(b), however, while all the (purple) carbon atoms remain sp^2-like, all the edge (white) carbon atoms become sp^3-like. The calculated band structures in Fig. 1(c) and (d) show that the green motif is a one-dimensional (1D) Weyl semimetal, while the purple motif is a semiconductor.

[a]*School of Physics and Optoelectronics, Xiangtan University, Xiangtan, 411105 Hunan, China. E-mail: chenyp@xtu.edu.cn, xieyech@xtu.edu.cn*
[b]*Research Laboratory for Quantum Materials, Singapore University of Technology and Design, Singapore 487372, Singapore*
[c]*Department of Physics, University of California at Berkeley, and Materials Sciences Division, Lawrence Berkeley National Laboratory, Berkeley, California 94720, USA*
[d]*Department of Physics, Applied Physics, and Astronomy Rensselaer Polytechnic Institute, Troy, New York 12180, USA. E-mail: zhangs9@rpi.edu*
†Electronic supplementary information (ESI) available. See DOI: 10.1039/c6nr00882h

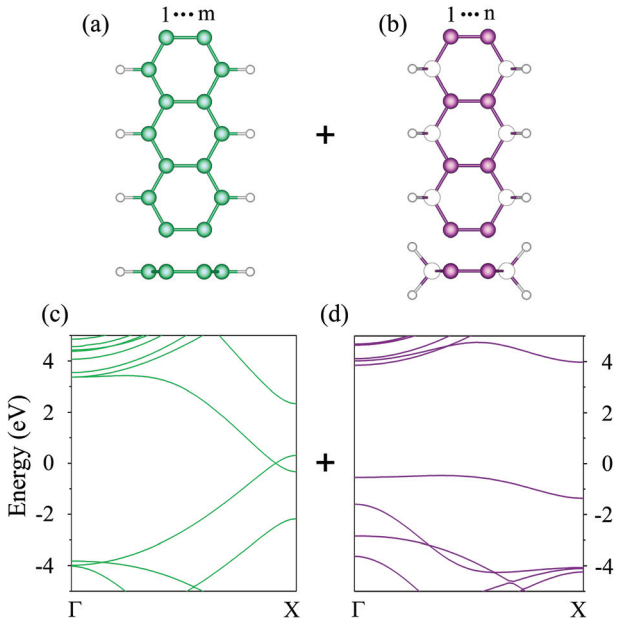

Fig. 1 (a, b) Two elemental building motifs of 3D graphene networks, which are both zigzag graphene nanoribbons. The widths of (a) the green and (b) the purple colored graphene nanoribbons are their respective numbers of zigzag chains, labeled here as m and n. Upon linking, atoms at the two edges of the purple colored nanoribbon (marked as hollow circles) are sp^3-hybrdizated. Also, hydrogen atoms (small hollow circles) are shown. They are used only for band structure calculations in (c, d) rather being part of the motifs. (c, d) Band structures of the two zigzag graphene nanoribbons in (a) and (b) with m = 2 and n = 2, respectively. No hydrogen states appear in this energy range.

Three families of graphene networks (shown in Fig. 2) may be constructed from these motifs, as various highly-ordered arrays of 1D Weyl semimetals. Such a unique arrangement, in contrast to the IGNs, lays the groundwork for novel correlated electronic phases such as charge density waves and spin density waves,[23–25] provided that the many-body correlation length is comparable or exceeds motif separations. Due to the huge density of states near the Fermi surface, superconducting instability with high T_c[26] may also arise. When cutting into slabs or nanowires in certain crystallographic directions, the Weyl electron characteristics remains robust and the surfaces states are usually flat, which opens the door to carbon-based high-temperature ferromagnetism.[27–29] A tight-binding model is developed to explain the mechanism underlying these unique electronic properties in terms of orbital interaction. In particular, the robustness of the Weyl semimetals is derived from a nontrivial topology, ensured by the sublattice symmetry, leading to an inverted band structure near the Fermi surface.

Results and discussion

The graphene networks in Fig. 2 may be classified as a triangular graphene network (TGN), quadrilateral graphene network (QGN), and hexagonal graphene network (HGN), respectively. By changing the width of the green nanoribbon (m) and purple nanoribbon (n), one arrives at the three families of graphene networks, TGN(m,n), QGN(m,n), and HGN(m,n). Table 1 shows the structural properties for these, where each type has three representative structures. The corresponding properties of

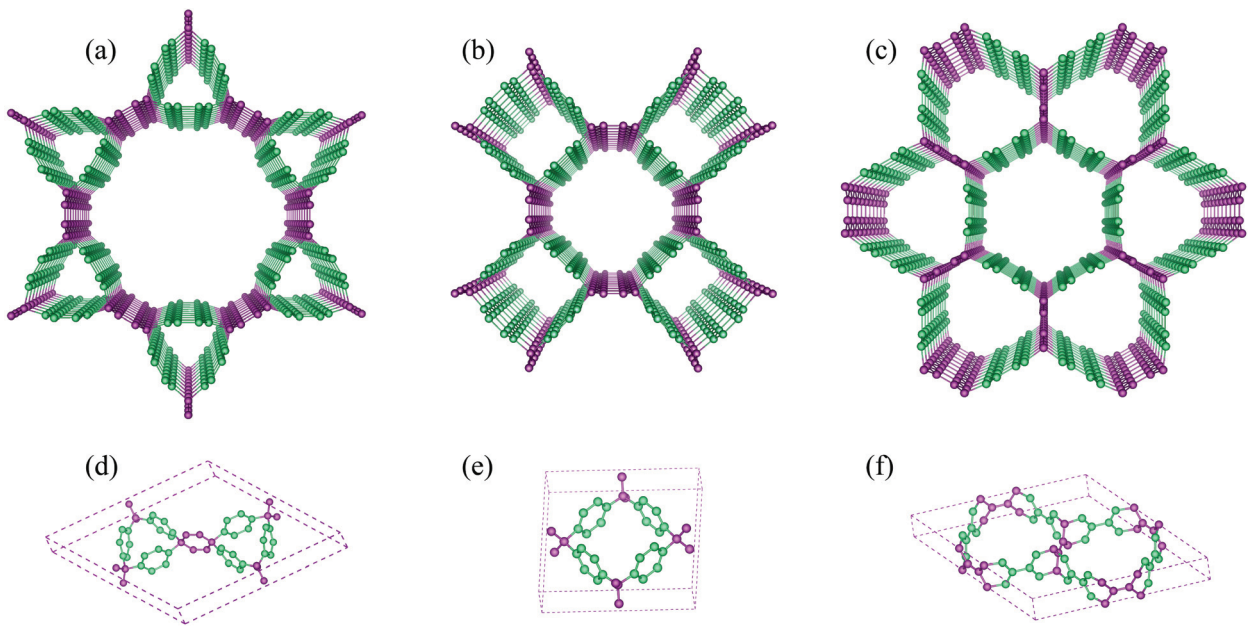

Fig. 2 3D graphene networks. (a–c) Top views of TGN(2,2), QGN(2,2), and HGN(2,2), with m = 2 and n = 2, as defined in the main text and in the caption for Fig. 1. (d–f) A tilted view of the unit cells corresponding to the graphene networks in (a–c).

Table 1 Structural properties for nine representative graphene networks, diamond, and graphite. They include the space group, density (g cm^{-3}), bond lengths (Å), bulk moduli (GPa), and cohesive energy E_{coh} (eV per atom)

System	m	n	Space group	Density	Bond lengths	Bulk Moduli	E_{coh}
TGN	2	1	$P6_3/mmc$	1.67	1.42, 1.45, 1.52	201.28	−7.70
	2	2	$P6/mmm$	1.21	1.34–1.54	144.11	−7.65
	2	3	$P6_3/mmc$	0.94	1.36–1.54	112.69	−7.66
QGN	1	2	$P4_2/mmc$	1.87	1.34–1.54	194.79	−7.60
	2	2	$P4/mmm$	1.51	1.34–1.53	151.46	−7.68
	2	4	$P4/mmm$	1.06	1.36–1.54	127.09	−7.69
HGN	1	3	$P6_3/mcm$	1.75	1.36–1.54	208.06	−7.61
	2	2	$P6/mmm$	1.54	1.34–1.53	184.26	−7.67
	2	4	$P6/mmm$	1.24	1.36–1.54	148.05	−7.68
Diamond			$Fd\bar{3}m$	3.55	1.54	431.32	−7.77
Graphite			$P6_3/mmc$	2.24	1.42	36.4	−7.90

graphite and diamond are also shown for comparison. One can see that the bond lengths in these structures are in the range of 1.36–1.54 Å. Most of them are between those of diamond (1.54 Å) and graphite (1.42 Å). The shorter-than-1.42 Å bonds are the sp^2-hybridized bonds inside the purple nanoribbons, whereas the longer-than-1.54 Å bonds are the sp^3-hybridized bonds between the green and purple nanoribbons. The porous structures here lead to small carbon densities which are even lower than that of graphite. On the other hand, all the 3D networks have much higher bulk moduli than that of graphite. The calculated cohesive energy E_{coh} indicates that these structures are all highly-stable carbon allotropes, as the E_{coh}'s are only 0.1–0.3 eV per C smaller than those of diamond and graphite. These values in Table 1 can be contrasted to other proposed low-density carbon allotropes, such as T-carbon[30] (−6.59 eV per C), Bct-C4[31] (−7.57 eV per C), CKL[15] (−7.49 eV per C), Y-carbon[32] (−6.75 eV per C), and TY-carbon[32] (−6.71 eV per C). To be more certain of the stability, we also calculated the phonon spectra and independent elastic constants. They are shown in Fig. S1 and Table S1 of the ESI.† We could not find any soft phonon modes over the entire Brillouin Zone (BZ), and all the independent elastic constants satisfy the Born stability criteria.[33]

Fig. 3 shows the band structures for TGN(2,2), QGN(2,2), and HGN(2,2), respectively. It is interesting to note that all the networks are semimetals with a Dirac linear dispersion near the Fermi level. Below, we take the simplest network, QGN(2,2) in Fig. 3(b), as an example to explain the electronic properties for all the three types. One observes from this figure that linear crossing points appear along each of the k paths, Γ–Z, A–M, and X–R. These Weyl-like points are marked on the BZ [inset of Fig. 3(b)] as three red dots, and, as a matter of fact, they are all on the reciprocal-space surface $k_z = 0.39\pi/c$, which forms a Weyl surface in the BZ for QGN(2,2). By time reversal symmetry, there should be another Weyl surface at $k_z = -0.39\pi/c$. Similar Weyl surfaces are also found for TGN(2,2) and HGN(2,2). In other words, all the graphene networks are semimetals with Weyl surfaces passing through their respective Fermi levels. Therefore, all the 3D carbon networks studied here can be termed as Weyl-surface semimetals. It should be noted that the Weyl surfaces identified here are distinct from the conventional

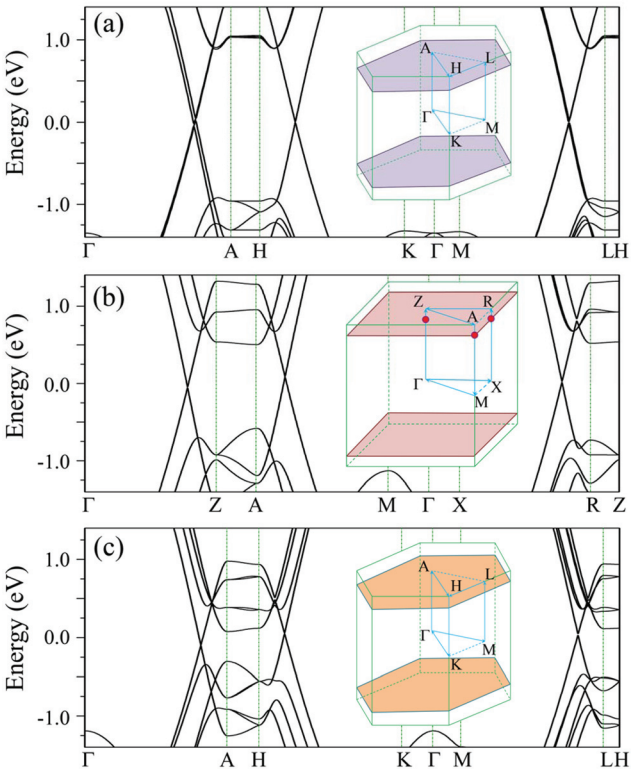

Fig. 3 Band structures of graphene networks near the Fermi level (which has been set to zero). (a) TGN(2, 2), (b) QGN(2, 2), and (c) HGN(2, 2). Insets are the corresponding BZs, with the Dirac surfaces marked in color. In (b), the three red dots in the inset are the positions of the Dirac points along the Γ–Z, A–M, and X–R paths, in the band structure plot.

Fermi surface of ordinary metals: a Weyl surface is formed by a linear crossing of two electronic bands hence the low-energy quasiparticles must be described by two-component Weyl spinors. Due to this added degeneracy, Weyl surfaces are typically not as stable as the conventional Fermi surfaces[34] (which explains why they are so rare), unless additional crystalline symmetries exist, as will be discussed below.

To understand the origin of the Weyl surfaces, we plot in Fig. 4(a) and (b) the band structure and partial density of states (PDOS) for QGN(1,2). The unit cell of the structure is

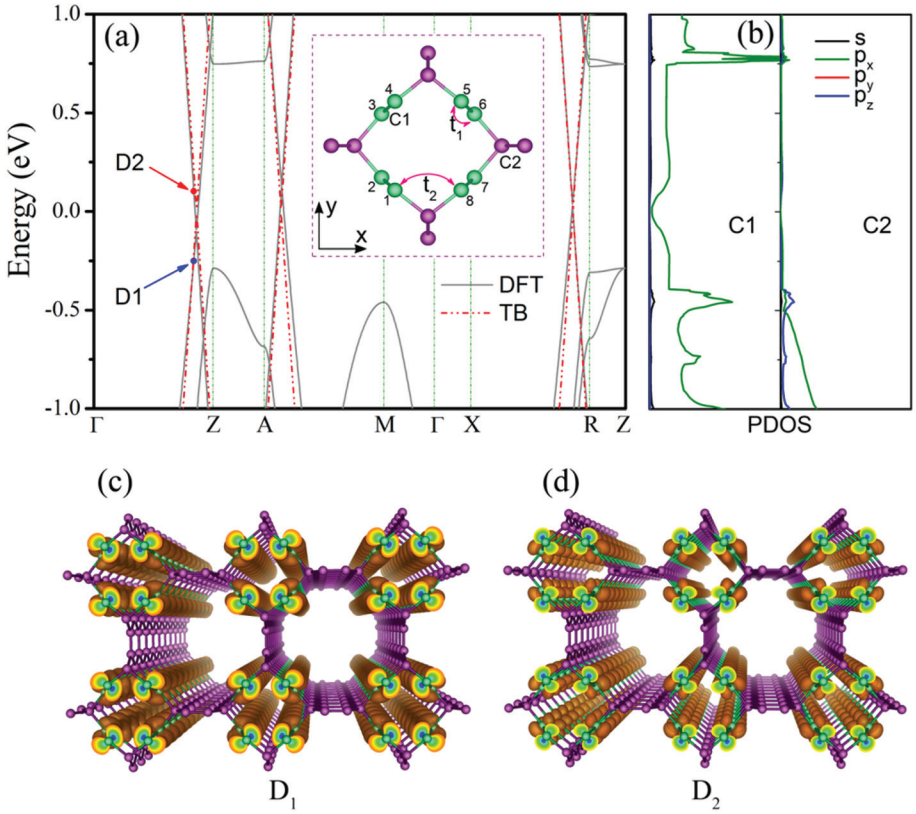

Fig. 4 (a) Band structure of QGN(1,2), given by DFT (solid lines) and TB model (dashed lines). Inset is the top view of the atomic structure for QGN (1,2), where (green) C1 and (purple) C2 represent the two kinds of atoms mentioned in Fig. 1. t_1 and t_2 are the intra- and inter-chain hopping energy parameters (t_1 = 2.95 eV and t_2 = 1.3 eV). (b) PDOS for the C1 and C2 atoms, respectively. (c, d) Charge densities for the states at the (blue) D_1 and (red) D_2 points in (a), respectively.

shown in the inset of Fig. 4(a), which consists of eight green atoms labeled C1 and eight purple atoms labeled C2. As mentioned above, in the graphene network the electronic states around the Fermi level are contributed to by the green-colored nanoribbons, while the function of the purple-colored nanoribbons is to provide the backbone of the structures. Therefore, the PDOS in Fig. 4(b) reveals that the Weyl bands around the Fermi level originated from states only on C1 atoms, with the relevant electron orbitals being p_x or p_y, rather than being p_z or s. As a comparison, Fig. 4(c) and (d) show the charge density profiles for the states in the Weyl bands. One can see that the charge density on a C1 atom corresponds to that of one π-orbital, which is very similar to that in an armchair carbon nanotube. Because the purple-colored zigzag nanoribbons have little contribution to the Weyl bands, we can omit them and, in the following discussion, just consider the green-colored zigzag nanoribbons, which in a unit cell form a closed cylinder just like a distorted armchair carbon nanotube. In this sense, the graphene network can be viewed as a 3D bundle of carbon nanotubes. It is known that the nanotubes are 1D Weyl semimetals with linearly crossing Fermi points in their respective band structures.[35] A simple physical picture is that, when forming the carbon networks, the inter-tube coupling between the σ electrons in the x–y plane is rather strong, leading to significant dispersions, but the inter-tube coupling between the π electrons in the same plane is vanishingly small, leading to Weyl surfaces which are almost dispersionless in the x–y plane.

Because only the π orbitals of the C1 atoms contribute to the Weyl surface properties of QGN(1,2), a tight-binding (TB) model, based on a single orbital per C1 site, can be used to describe its properties around the Fermi level,

$$H = \sum_{<i,j>} \sum_{\mu} t_{ij} e^{-i\mathbf{k}\cdot\mathbf{d}_{ij}^{\mu}} \quad (1)$$

where $i, j \in 1, 2, \ldots, 8$ are the eight C1 sites as in the inset of Fig. 4(a), $\mathbf{d}_{ij}^{\mu}$ is a vector directed from j to i, t_{ij} is the hopping energy between i and j, and μ runs over all equivalent lattice sites under translation. For t_{ij}, we only consider two hopping processes: one is the nearest-neighbor interaction inside one zigzag nanoribbon t_1; the other is between the nearest sites of two neighboring green nanoribbons t_2 as indicated in the inset of Fig. 4(a). The spectrum of the energy band is symmetric about zero energy because of the presence of a sublattice symmetry with two sublattices of sites {1,3,5,7} and {2,4,6,8} respectively. Eqn (1) can be easily diagonalized to yield

$$(\lambda - x_0)(\lambda + x_1)^2(\lambda - x_2) = 0 \quad (2)$$

where $\lambda = E^2$, $x_0 = [2t_1\cos(k_c c/2) + t_2]^2$, $x_1 = -[4{t_1}^2\cos^2(k_c c/2) + {t_2}^2]$ and $x_2 = [2t_1\cos(k_c c/2) - t_2]^2$. It is straightforward to find that zero-energy states would appear if $x_0 = 0$ or $x_2 = 0$, *i.e.*, $\cos(k_c c/2) = \pm\frac{t_2}{2t_1}$. Because we should have $t_2 < t_1$, the zero-energy states appear on two separate surfaces at $k_z = K_c \equiv \pm(2/c)\arccos\left[\sqrt{t_2/(2t_1)}\right]$. Despite its simplicity, the model captures the essential physics of the first-principles results. In Fig. 4(a), the fitted band structure of the tight-binding model is also shown, which agrees rather well with first-principles results. Around the Weyl surface at $\tau_z K_c(\tau_z = \pm 1)$, the low-energy quasiparticles are described by the effective Hamiltonian

$$H_{\text{eff}}(q_z) = \tau_z v q_z \sigma_z \tag{3}$$

where $q_z = k_z - K_c$ is the wave vector component normal to the Weyl surface, $v \approx 1.0 \times 10^6$ m s^{-1} is the Fermi velocity, and the Pauli matrix σ_z denotes the two bands crossing at the surface. For each surface, eqn (3) takes the form of a 1D Weyl Hamiltonian, and the chirality reverses between the two surfaces as required by the time reversal symmetry. These are the essential features of Weyl-surface semimetals.

As mentioned, the Weyl surface is in general not stable unless it has symmetry/topology protection. For the structures studied here, the stability is closely related to their sublattice symmetry, which is ensured, for example, by the crystalline mirror symmetries inherent to the structure along the x or y axis or a combination of the two. With negligible spin-orbit coupling for carbon, such systems fall into the BDI topological class with a zero-dimensional $\mathbb{Z}_2$ topological invariant defined at any point in the BZ with a local gap.[36–38] The $\mathbb{Z}_2$ invariant just indicates whether the gap is inverted or not, with reference to the normal band ordering in the atomic limit. In the graphene networks, the band gap is inverted $(\mathbb{Z}_2 = 1)$ near the central region of BZ while it is un-inverted $(\mathbb{Z}_2 = 0)$ around Z-point at the BZ boundary, hence the Weyl surfaces which separates the two regions with different band topologies cannot be gapped as long as the sublattice symmetry is maintained.

We find that under both uniaxial and biaxial strains, the mirror symmetry and hence the sublattice symmetry is preserved in the graphene networks. Therefore, when a uniaxial/biaxial compressive strain is applied to the structure, the Weyl surfaces simply shift their positions to the center of the BZ; when a uniaxial/biaxial tensile strain is applied, on the other hand, the Dirac surfaces will shift in the opposite direction (see Fig. S2 of the ESI†). It is only when the sublattice symmetry is broken that the Dirac surfaces would be destroyed and the system is gapped or becomes metallic. However, this symmetry breaking is difficult because the networks are strongly against such distortions, as revealed by their share

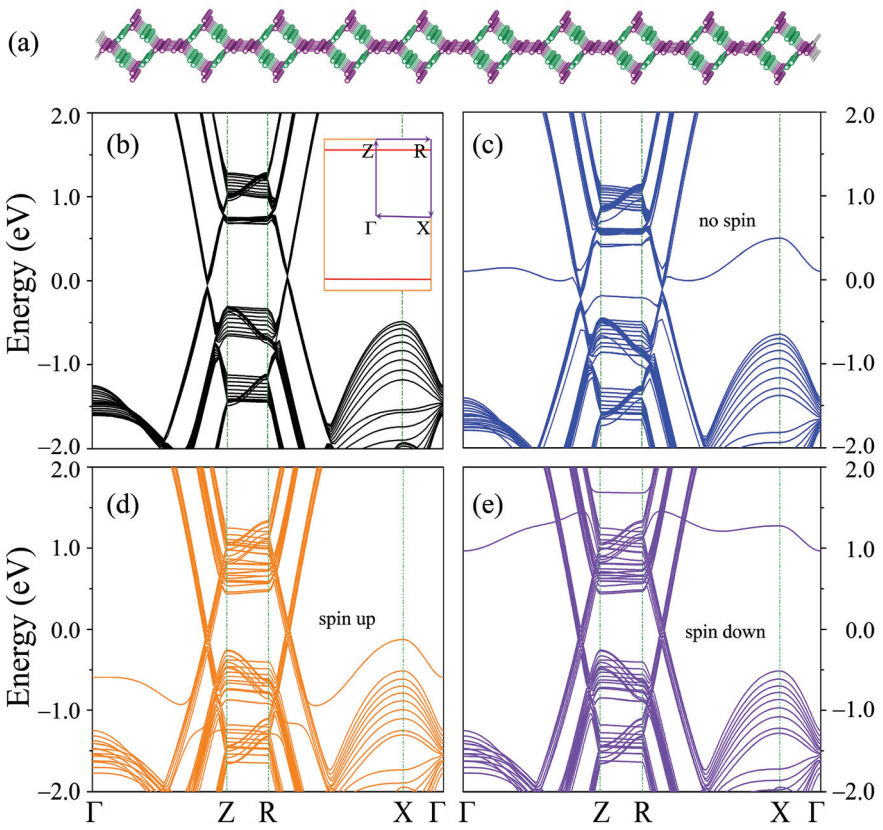

Fig. 5 (a) Atomic structure of a 10-layer thick slab of QGN(1,2). Each atom on the surface is passivated by two hydrogen atoms. (b) Corresponding band structure. Inset shows the BZ where two red lines represent the two Dirac lines. (c) Non-spin-polarized band structure of the 10-layer thick slab when each atom on the surfaces is passivated by only one hydrogen atom. (d, e) Corresponding spin-polarized band structures for (c).

moduli in Table S1.† Therefore, the Weyl surfaces in the graphene networks are quite robust.

When the 3D graphene network is cut in parallel to the zigzag-chain directions, a slab will be obtained. Fig. 5(a) shows a 10-layer slab for QGN(1,2), where for the ease of discussion, each carbon atom on the surfaces is passivated by two hydrogen atoms. Fig. 5(b) shows the band structure of the slab, from which one can see two linearly crossing points at the Fermi level. A closer examination reveals that the cut leads to two Weyl lines on the 2D BZ, as shown in the inset of Fig. 5(b). Therefore, the slab is also a Weyl-line semimetal, whose Weyl lines can be understood either as a projection of the Weyl surfaces from a 3D BZ to a 2D BZ, or as an expansion of the 1D Weyl points (of isolated nanotubes) in a 1D BZ to a 2D BZ. Here, the purpose of the passivation by hydrogen is only to eliminate the dangling bonds at the surfaces. It should not have any effect on the physics of most of the Weyl electrons, which mainly reside inside the slab. It is, however, interesting to consider what might happen when each carbon atom on the surface is passivated by only one hydrogen atom, which would expose one of the surface states with no hydrogen passivation. Fig. 5(c) shows the corresponding band structure, calculated without spin polarization. A rather flat and half-occupied surface band appears that connects the two Weyl points near the Fermi level. It is known that in a flat band, there could be strong electron correlation effects.[29,39–42] Fig. 5(d) and (e) show that, when the electron spin is considered, the flat band splits into a spin-up and a spin-down band, leading to surface ferromagnetism. Interestingly, the Weyl electrons do not participate in the magnetism, nor are the majority of them affected by the presence of the surface ferromagnetism due to their strong localization within individual nanotubes.

When the 2D slabs are further cut, 1D nanowires are obtained. Similar to the 2D slabs, the electronic properties of the nanowires here also depend on the surface passivation. Fig. 6(a) shows the calculated band structure when each surface atom is passivated by two hydrogen atoms. Clearly, the nanowires are 1D Weyl-point semimetals. Fig. 6(b) shows the non-spin polarized band structure, when each surface atom is passivated by only one hydrogen atom. In this case, a number of rather flat surface and near-surface bands appear near the Fermi level. As expected, Fig. 6(c) and (d) reveal that the spin-polarization has a significant effect on these bands, again leading to surface ferromagnetism.

The Weyl lines/points in the 2D/1D graphene networks as well as the appearance of flat surface bands are also derived from the topological properties of the bulk band structure. For example, similarly to the Weyl surfaces, the surfaces of the 3D network structures also represent an interface separating the gap-inverted nontrivial region and the (trivial) vacuum; hence surface bands exist in between the projected Weyl surfaces on the side surfaces, as observed in Fig. 5(c). Because the sublattice symmetry may not be retained at the system boundary, the surface bands could be distorted from being flat or even pushed away from the Fermi level depending on the boundary conditions, in analogy with the edge states of graphene.[43]

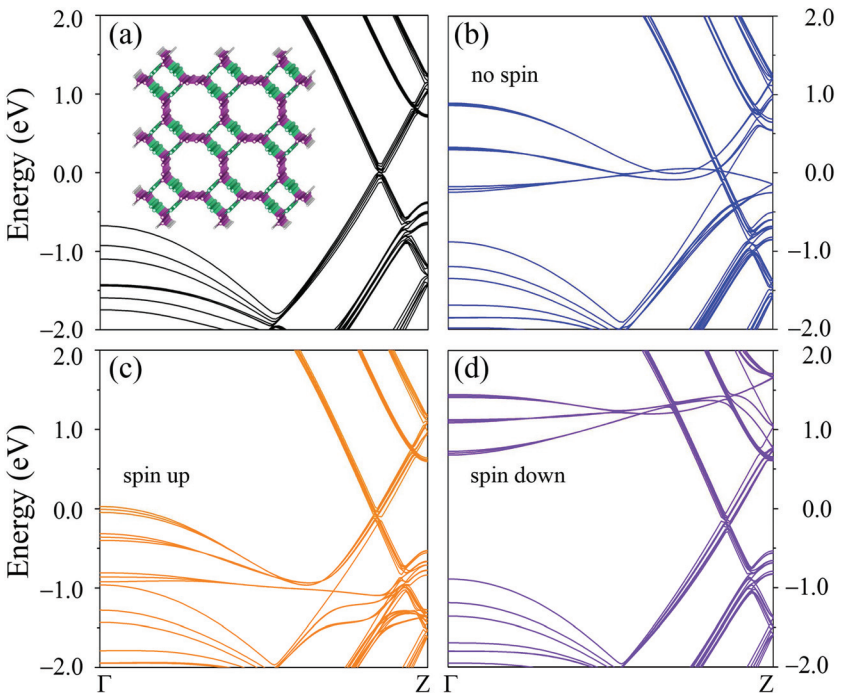

Fig. 6 Band structure for the nanowire obtained by cutting a 3 × 3 unit cell out of QGN(1,2). (a) When each atom on the surfaces is passivated by two hydrogen atoms. Inset shows the atomic structure. (b) When each atom on the surfaces is passivated by only one hydrogen atom (non-spin-polarized). (c, d) Same as (b) but with spin polarization.

Conclusions

Using a combination of sp^2 and sp^3 carbon atoms as examples, we have systematically studied possible Weyl structures in the solid state. In particular, we determine that graphene is a 2D Weyl semimetal with a Dirac cone and a carbon zigzag chain is a 1D Weyl semimetal with a Dirac cross. The 1D chains are the building motifs for both 2D and 3D Weyl semimetals. We further demonstrate that the family of 3D Weyl semimetals consists of not only those known structures with Weyl points, and Weyl loops, but, in the extreme case, also those with Weyl surfaces at the Fermi level when the carbon network forms a 3D bundle of zero-gap nanotubes connected by gapped nanoribbons. The real-space bundle structure and the exceptionally large density of states near the Fermi level offer unique opportunities for studying correlated many-body effects. One may cut the 3D networks into 2D Weyl slabs or 1D Weyl nanowires. If each carbon atom on the surfaces is passivated, surface ferromagnetism will result due to a strong Coulomb repulsion between localized electrons. A tight-binding model is constructed, which allows us to explain most of the salient features predicted by first-principles calculations. We note that a recent experiment showed[44] the possibility of growing 3D carbon foams with vertical channels by a deposition of vacuum-sublimated graphite. Their structure is quite similar to what has been proposed here, although more work is needed to conclusively determine the atomic structure. Regardless, the realization of Weyl-surface materials can be expected in the near future.

Methods

We performed first-principles calculations within density functional theory (DFT) as implemented in VASP codes.[45] The potential of the core electrons and the exchange–correlation interaction between the valence electrons were described, respectively, by the projector augmented wave[46] and the generalized gradient approximation (GGA) with a Perdew-Burke-Ernzerhof (PBE) functional.[47] A kinetic energy cutoff of 500 eV was used. The atomic positions were optimized using the conjugate gradient method, and the energy and force convergence criteria were set to be 10^{-5} eV and 10^{-2} eV Å^{-1}, respectively. In the calculations of the slab geometry, the two nearest slabs were separated by a vacuum layer of at least 10 Å to avoid artificial interactions. To sample the BZ, we used *k*-point grids with a spacing $2\pi \times 0.02$ Å^{-1} for tetragonal systems and a Γ-centered sampling scheme for hexagonal systems, respectively, within the Monkhorst–Pack sampling scheme.[48]

Acknowledgements

This work was supported by the National Natural Science Foundation of China (No. 51176161, 51376005 and, 11474243) and the Hunan Provincial Innovation Foundation for Postgraduate (No. CX2015B211). SAY was supported by SUTD-SRG-EPD2013062 and SUTD-T1-2015004. MLC was supported by the sp^2 bonded materials program at the Lawrence Berkeley National Lab through the Office of Basic Energy Sciences, U.S. Department of Energy under Contract No. DE-AC02-05CH11231, and by the National Science Foundation under Grant No.DMR15-1508412. SBZ acknowledges support by US DOE under Grant No. DE-SC0002623.

References

1 S. Y. Xu, I. Belopolski, N. Alidoust, M. Neupane, G. Bian, C. Zhang, R. Sankar, G. Chang, Z. Yuan, C. C. Lee, S. M. Huang, H. Zheng, J. Ma, D. S. Sanchez, B. Wang, A. Bansil, F. Chou, P. P. Shibayev, H. Lin, S. Jia and M. Z. Hasan, *Science*, 2015, **349**, 613–617.
2 A. A. Soluyanov, D. Gresch, Z. Wang, Q. Wu, M. Troyer, X. Dai and B. A. Bernevig, *Nature*, 2015, **527**, 495–498.
3 B. Q. Lv, H. M. Weng, B. B. Fu, X. P. Wang, H. Miao, J. Ma, P. Richard, X. C. Huang, L. X. Zhao, G. F. Chen, Z. Fang, X. Dai, T. Qian and H. Ding, *Phys. Rev. X*, 2015, **5**, 031013.
4 H. Weng, C. Fang, Z. Fang, B. A. Bernevig and X. Dai, *Phys. Rev. X*, 2015, **5**, 011029.
5 B. Q. Lv, N. Xu, H. M. Weng, J. Z. Ma, P. Richard, X. C. Huang, L. X. Zhao, G. F. Chen, C. E. Matt, F. Bisti, V. N. Strocov, J. Mesot, Z. Fang, X. Dai, T. Qian, M. Shi and H. Ding, *Nat. Phys.*, 2015, **11**, 724–727.
6 L. X. Yang, Z. K. Liu, Y. Sun, H. Peng, H. F. Yang, T. Zhang, B. Zhou, Y. Zhang, Y. F. Guo, M. Rahn, D. Prabhakaran, Z. Hussain, S. K. Mo, C. Felser, B. Yan and Y. L. Chen, *Nat. Phys.*, 2015, **11**, 728–732.
7 X. Wan, A. M. Turner, A. Vishwanath and S. Y. Savrasov, *Phys. Rev. B: Condens. Matter*, 2011, **83**, 205101.
8 S.-Y. Xu, N. Alidoust, I. Belopolski, Z. Yuan, G. Bian, T.-R. Chang, H. Zheng, V. N. Strocov, D. S. Sanchez, G. Chang, C. Zhang, D. Mou, Y. Wu, L. Huang, C.-C. Lee, S.-M. Huang, B. Wang, A. Bansil, H.-T. Jeng, T. Neupert, A. Kaminski, H. Lin, S. Jia and M. Zahid Hasan, *Nat. Phys.*, 2015, **11**, 748–754.
9 E. D. Miller, D. C. Nesting and J. V. Badding, *Chem. Mater.*, 1997, **9**, 18–22.
10 A. Hirsch, *Nat. Mater.*, 2010, **9**, 868–871.
11 A. H. Castro Neto, N. M. R. Peres, K. S. Novoselov and A. K. Geim, *Rev. Mod. Phys.*, 2009, **81**, 109–162.
12 K. S. Novoselov, A. K. Geim, S. V. Morozov, D. Jiang, M. I. Katsnelson, I. V. Grigorieva, S. V. Dubonos and A. A. Firsov, *Nature*, 2005, **438**, 197–200.
13 Y. Yao, F. Ye, X.-L. Qi, S.-C. Zhang and Z. Fang, *Phys. Rev. B: Condens. Matter*, 2007, **75**, 041401.
14 Q. Li, Y. Ma, A. R. Oganov, H. Wang, H. Wang, Y. Xu, T. Cui, H. K. Mao and G. Zou, *Phys. Rev. Lett.*, 2009, **102**, 175506.
15 Y. Chen, Y. Y. Sun, H. Wang, D. West, Y. Xie, J. Zhong, V. Meunier, M. L. Cohen and S. B. Zhang, *Phys. Rev. Lett.*, 2014, **113**, 085501.

16 A. Liu, M. Cohen, K. Hass and M. Tamor, *Phys. Rev. B: Condens. Matter*, 1991, **43**, 6742–6745.
17 R. Hoffmann, T. Hughbanks, M. Kertesz and P. H. Bird, *J. Am. Chem. Soc.*, 1983, **105**, 4831–4832.
18 S. Zhang, Q. Wang, X. Chen and P. Jena, *Proc. Natl. Acad. Sci. U. S. A.*, 2013, **110**, 18809–18813.
19 D. L. V. K. Prasad, N. M. Gerovac, M. J. Bucknum and R. Hoffmann, *J. Chem. Theory Comput.*, 2013, **9**, 3855–3859.
20 H. Weng, Y. Liang, Q. Xu, R. Yu, Z. Fang, X. Dai and Y. Kawazoe, *Phys. Rev. B: Condens. Matter*, 2015, **92**, 045148.
21 Y. Chen, Y. Xie, S. A. Yang, H. Pan, F. Zhang, M. L. Cohen and S. Zhang, *Nano Lett.*, 2015, **15**, 6974–6978.
22 Z. Chen, W. Ren, L. Gao, B. Liu, S. Pei and H. M. Cheng, *Nat. Mater.*, 2011, **10**, 424–428.
23 G. Grüner, *Rev. Mod. Phys.*, 1988, **60**, 1129–1181.
24 J. E. Hirsch, *Phys. Rev. Lett.*, 1984, **53**, 2327–2330.
25 O. A. Starykh and L. Balents, *Phys. Rev. B: Condens. Matter*, 2014, **89**, 104407.
26 N. B. Kopnin, T. T. Heikkila and G. E. Volovik, *Phys. Rev. B: Condens. Matter*, 2011, **83**, 220503.
27 R. L. Doretto and M. O. Goerbig, *Phys. Rev. B: Condens. Matter*, 2015, **92**, 245124.
28 N. Shima and H. Aoki, *Phys. Rev. Lett.*, 1993, **71**, 4389–4392.
29 Z. Liu, F. Liu and Y.-S. Wu, *Chin. Phys. B*, 2014, **23**, 077308.
30 X. L. Sheng, Q. B. Yan, F. Ye, Q. R. Zheng and G. Su, *Phys. Rev. Lett.*, 2011, **106**, 155703.
31 K. Umemoto, R. M. Wentzcovitch, S. Saito and T. Miyake, *Phys. Rev. Lett.*, 2010, **104**, 125504.
32 J. Y. Jo and B. G. Kim, *Phys. Rev. B: Condens. Matter*, 2012, **86**, 075151.
33 Z.-j. Wu, E.-j. Zhao, H.-p. Xiang, X.-f. Hao, X.-j. Liu and J. Meng, *Phys. Rev. B: Condens. Matter*, 2007, **76**, 054115.
34 G. E. Volovik, *The Universe in a Helium Droplet*, Clarendon Press, Oxford, 2003.
35 O. Gülseren, T. Yildirim, S. Ciraci and Ç. Kılıç, *Phys. Rev. B: Condens. Matter*, 2002, **65**, 155410.
36 A. P. Schnyder, S. Ryu, A. Furusaki and A. W. W. Ludwig, *Phys. Rev. B: Condens. Matter*, 2008, **78**, 195125.
37 S. Matsuura, P.-Y. Chang, A. P. Schnyder and S. Ryu, *New J. Phys.*, 2013, **15**, 065001.
38 J. C. Y. Teo and C. L. Kane, *Phys. Rev. B: Condens. Matter*, 2010, **82**, 115120.
39 C. Wu, D. Bergman, L. Balents and S. Das Sarma, *Phys. Rev. Lett.*, 2007, **99**, 070401.
40 A. P. Schnyder and S. Ryu, *Phys. Rev. B: Condens. Matter*, 2011, **84**, 060504.
41 C. Weeks and M. Franz, *Phys. Rev. B: Condens. Matter*, 2012, **85**, 041104.
42 H. Tamura, K. Shiraishi, T. Kimura and H. Takayanagi, *Phys. Rev. B: Condens. Matter*, 2002, **65**, 085324.
43 Y. Wang, S. A. Yang and Q. Niu, *Phys. Rev. Lett.*, 2009, **102**, 096801.
44 N. V. Krainyukova and E. N. Zubarev, *Phys. Rev. Lett.*, 2016, **116**, 055501.
45 G. Kresse and J. Hafner, *Phys. Rev. B: Condens. Matter*, 1993, **47**, 558–561.
46 G. Kresse and D. Joubert, *Phys. Rev. B: Condens. Matter*, 1999, **59**, 1758–1775.
47 J. P. Perdew, J. A. Chevary, S. H. Vosko, K. A. Jackson, M. R. Pederson, D. J. Singh and C. Fiolhais, *Phys. Rev. B: Condens. Matter*, 1992, **46**, 6671–6687.
48 H. J. Monkhorst and J. D. Pack, *Phys. Rev. B: Solid State*, 1976, **13**, 5188–5192.